

Atomic insights into topochemical fluorination and strong octahedral tilt in La_2CoO_4

Yuzhou He(何玉洲), Ting Lin(林挺), Shiyu Wang(王诗雨), Ang Gao(高昂), Ziang Meng(孟子昂), Tianping Ying(应天平), Zhiqi Liu(刘知琪), Lin Gu(谷林), Qinghua Zhang(张庆华), and Binghui Ge(葛炳辉)
Citation: Chin. Phys. B, 2025, 34 (**7**): 076102. DOI: 10.1088/1674-1056/adda0a
http://cpb.iphy.ac.cn; http://iopscience.iop.org/cpb

What follows is a list of articles you may be interested in

High-burn-up structure evolution in polycrystalline UO_2: Phase-field modeling investigation

Dan Sun(孙丹), Yanbo Jiang(姜彦博), Chuanbao Tang(唐传宝), Yong Xin(辛勇), Zhipeng Sun(孙志鹏), Wenbo Liu(柳文波), and Yuanming Li(李垣明)
Chin. Phys. B, 2025, 34 (**2**): 026102. DOI: 10.1088/1674-1056/ad9c42

Pressure-induced superconductivity and phase transition in PbSe and PbTe

Yuyang Jiang(江宇阳), Cuiying Pei(裴翠颖), Qi Wang(王琦), Juefei Wu(吴珏霏), Lili Zhang(张丽丽), Chao Xiong(熊超), and Yanpeng Qi(齐彦鹏)
Chin. Phys. B, 2024, 33 (**12**): 126105. DOI: 10.1088/1674-1056/ad8ecc

Pressure-induced novel structure with graphene-like boron-layer in titanium monoboride

Yuan-Yuan Jin(金园园), Jin-Quan Zhang(张金权), Shan Ling(凌山), Yan-Qi Wang(王妍琪), Song Li(李松), Fang-Guang Kuang(匡芳光), Zhi-Yan Wu(武志燕), and Chuan-Zhao Zhang(张传钊)
Chin. Phys. B, 2022, 31 (**11**): 116104. DOI: 10.1088/1674-1056/ac9222

Structural evolution and molecular dissociation of H_2S under high pressures

Wen-Ji Shen(沈文吉), Tian-Xiao Liang(梁天笑), Zhao Liu(刘召), Xin Wang(王鑫), De-Fang Duan(段德芳), Hong-Yu Yu(于洪雨), and Tian Cui(崔田)
Chin. Phys. B, 2022, 31 (**7**): 076102. DOI: 10.1088/1674-1056/ac5980

Effect of tellurium (Te^{4+}) irradiation on microstructure and associated irradiation-induced hardening

Hefei Huang(黄鹤飞), Jizhao Liu(刘继召), Guanhong Lei(雷冠虹), Ondrej Muránsky, Tao Wei, and Mihail Ionescu
Chin. Phys. B, 2021, 30 (**5**): 056108. DOI: 10.1088/1674-1056/abf039

RAPID COMMUNICATION

Atomic insights into topochemical fluorination and strong octahedral tilt in La_2CoO_4

Yuzhou He(何玉洲)[1,2,†], Ting Lin(林挺)[3,†], Shiyu Wang(王诗雨)[2], Ang Gao(高昂)[2,4], Ziang Meng(孟子昂)[5], Tianping Ying(应天平)[2], Zhiqi Liu(刘知琪)[5], Lin Gu(谷林)[3], Qinghua Zhang(张庆华)[2,‡], and Binghui Ge(葛炳辉)[1,§]

[1] *Information Materials and Intelligent Sensing Laboratory of Anhui Province, Key Laboratory of Structure and Functional Regulation of Hybrid Materials of Ministry of Education, Institutes of Physical Science and Information Technology, Anhui University, Hefei* 230601, *China*

[2] *Beijing National Laboratory for Condensed Matter Physics, Institute of Physics, Chinese Academy of Sciences, Beijing* 100190, *China*

[3] *Beijing National Center for Electron Microscopy and Laboratory of Advanced Materials, Department of Materials Science and Engineering, Tsinghua University, Beijing* 100084, *China*

[4] *Institute of Environmental and Applied Chemistry, College of Chemistry, Central China Normal University, Wuhan* 430079, *China*

[5] *School of Materials Science and Engineering, Beihang University, Beijing* 100191, *China*

(Received 11 March 2025; revised manuscript received 22 April 2025; accepted manuscript online 19 May 2025)

Topochemical fluorination introduces significant structural distortions and emerging properties in perovskite oxides via substituting oxygen with fluorine. However, the rapid fluorination process and the similarity between F and O render the O/F site occupation and local lattice evolution during fluorination unclear. Here we investigated the atomic-scale O/F exchange in La_2CoO_4 and quantified the lattice distortion of three ordered structures: $La_2CoO_{3.5}F$, $La_2CoO_3F_2$, and $La_2CoO_{2.5}F_3$ by utilizing aberration-corrected electron microscopy. Atomic-resolved elemental mapping provides direct evidence for the O/F occupancy in interstitial and apical sites. We revealed that apical F ions induce significant octahedral tilting from 178° to 165°, linearly proportional to the occupancy rate; and cause the obvious change in the fine structure O *K* edge, meanwhile apical O is exchanged into interstitial sites. The strong octahedral tilt leads to the in-plane elongation of the $[CoO_4F_2]$ octahedra. These findings elucidate the atomic-scale mechanisms of the entire fluorination process and highlight the significant role of F in tuning the octahedral tilt of functional oxides.

Keywords: topochemical fluorination, structural evolution, octahedral tilting

PACS: 61.50.Ah, 68.37.Ma, 71.20.–b

DOI: 10.1088/1674-1056/adda0a **CSTR:** 32038.14.CPB.adda0a

1. Introduction

Anion regulation is an effective approach to explore new physical properties and structure–property relationships of transition metal oxides.[1–3] It introduces variations in both the valence states of transition metals and coordination environments. The partial substitution of O^{2-} with anions such as N^{3-}, H^-, or X^- (halide ions) can lead to significant lattice modifications and induce exotic phenomena such as photocatalysis,[4] ionic conductivity,[5] magnetization.[6] Topochemical fluorination substitutes oxygen with fluorine, which can effectively modifies oxygen octahedra and induces fascinating properties in perovskite oxides such as multiferroicity[7–9] and superconductivity.[10,11] Anion replacement breaks the inversion symmetry of the host lattice, thereby inducing ferroelectricity through cooperative tilting distortions in $La_3Ni_2O_{5.5}F_{3.5}$,[8] and large magnetic moment of the high-spin Co^{2+} ions in axially elongated CoO_4X_2 octahedra (where X = Cl, Br, S, Se).[12] F substitution can also exhibit site ordering and form a pyramidal coordination in Sr_2FeO_3F,[13] leading to significant distortion of the octahedra, rather than disordered apical O/F sites in K_2NbO_3F.[14] By introducing interstitial anions, $Sr_2CuO_2F_{2+\delta}$ achieves a structural reorganization and thereby produces the superconductivity.[10] As a result, atomic occupancy of O/F and its ordering are critical for structural distortions and novel electronic structures.

However, the rapid fluorination process and difficulties in distinguishing fluorine from oxygen render the structural evolution during fluorination unclear. Previous studies have adopted averaged characterization methods such as x-ray/neutron diffraction and x-ray photoelectron spectroscopy to determine the crystal structure and composition of oxyfluorides.[15–19] It was reported that there are two unknown intermediates before reaching the reaction temperature of 370 °C in La_2NiO_4.[16] Moreover, there is a big challenge in distinguishing fluorine and oxygen occupancy

†These authors contributed equally to this work.
‡Corresponding author. E-mail: zqh@iphy.ac.cn
§Corresponding author. E-mail: bhge@ahu.edu.cn

© 2025 Chinese Physical Society and IOP Publishing Ltd. All rights, including for text and data mining, AI training, and similar technologies, are reserved.

by neutron and x-ray diffractions because F and O have nearly identical atomic scattering factors.[20] Although fluoride ions are assumed in both the interstitial and apical positions in $Sr_2TiO_3F_2$,[18] $Ba_2ZrO_3F_2$[21] and $Ca_2CuO_2F_{2+\delta}$,[22] it is hard to assign the type of anion only by the analysis of the bond length.[23] Thus, it is desirable to directly visualize the local atomic structure and identify the anion occupancy of oxyfluorides in real space.

Here we combine aberration-corrected electron microscopy (STEM) and electron energy loss spectra (EELS) to investigate the structure evolution of La_2CoO_4 upon fluorination at atomic scale. Three ordered structures ($La_2CoO_{3.5}F$, $La_2CoO_3F_2$, and $La_2CoO_{2.5}F_3$) are revealed. A newly identified intermediate phase $La_2CoO_{3.5}F$ completes the entire pathway of the substitution dynamics. Atomically-resolved elemental mapping provides direct evidence for the O/F occupancy in interstitial and apical interstitial sites. The key role of apical F ions in determining octahedral tilt has been visualized, which is linearly proportional to the quantity of F ions and induces obvious change in the fine structure O *K* edge. These findings provide atomic insights into the entire process of O/F exchange and highlight the important role of F in tuning octahedral tilt, laying a foundation for the anion regulation in perovskite oxides.

2. Methods

2.1. Sample synthesis

The precursor oxide used in this experiment was prepared as a $La_2CoO_{4\pm d}$ thin film with a thickness of 37 nm on a (001) oriented single crystal MgO substrate at 750 °C and an oxygen partial pressure of 10^{-6} Torr using a pulsed laser deposition system with a base pressure of 3×10^{-8} Torr. After preparation, the film was thinned to a size suitable for TEM characterization using a focused ion beam system FEI Helios Nanolab 600i, resulting in a lamella of 5×1 μm which was placed on a FIB support, with the lamella thickness of about 40–50 nm. Topochemical low-temperature fluorination involved placing polyvinylidene fluoride (PVDF) and La_2CoO_4 lamellae at varying spacings within a quartz tube, followed by heating in a tubular furnace at 250 °C for 5 hours. This process generates F_2 gas, yielding compounds with controlled fluorination degrees.

2.2. STEM characterizations

The structural evolution upon fluorination was characterized by a spherical aberration-corrected transmission electron microscope, the JEM NeoARM200 (JEOL Ltd., Tokyo) operated at an acceleration voltage of 200 kV. STEM imaging and EELS analyses were performed with a probe convergence angles of 20 mrad and 28 mrad, resulting in probe sizes of 0.8 Å and 1.0 Å, respectively. Collection angles for high-angle annular dark-field (HAADF) and annular bright-field (ABF) images were 75–310 mrad and 11–23 mrad, respectively. A collection semiangle of 111 mrad was used for EELS investigations. For the acquisition of electron energy-loss spectroscopy (EELS) line scans and area scans, we utilized a GIF Continuum 1069 with the K3 direct electron detection camera to record the EELS spectra, which is well-suited for low-dose imaging and *in situ* studies, enabling the resolution of high-quality atomic structures even at low signal intensities.

2.3. Data processing

The critical bond angles and interlayer spacings calculated in this article are based on the atomic column positions mapped by Calatom software and the O-O Picker plugin.[24] The simulation of ABF images was obtained through Dr. Probe simulation software.[25] EELS data were processed with a multivariate weighted principal component analysis routine (MSA Plugin in Digital Micrograph) to decrease the noise level.

3. Results and discussion

3.1. Atomic structure of La_2CoO_4 and fluorination setup

The structure of the Ruddlesden–Popper (R-P) oxide A_2BO_4 provides rich sites for fluoride ion regulation.[26] As shown in Fig. 1(a), La_2CoO_4 consists of alternating perovskite ($LaCoO_3$) and rock-salt layers (LaO), where the perovskite layer contains equatorial (X1) and apical (X2) anionic sites, while the rock-salt layer contains interstitial anion sites (X3), providing plenty of room for anion regulation.[19,27] It can also work as a cathode material for fluoride ion batteries via F ion intercalation, significantly preventing irreversible side reactions during the fluorination process.[28] Epitaxial $La_2CoO_{4\pm x}$ thin films were reported as a novel type of ferromagnetic insulating oxide material with interstitial O exhibiting an exceptionally high Curie temperature ($T_c = 820$ K).[29] The atomic structure of the La_2CoO_4 films was investigated using high-angle annular dark-field (HAADF) imaging, showcasing the classic R-P structure and high-quality crystallinity.[30] The alternative stacking of [$LaCoO_3$] perovskite layer and [LaO] rock-salt layers can be visualized clearly in the $[100]_{pc}$ (pc is the abbreviation for pseudo cubic) projection; the [CoO_6] octahedra in the $[110]_{pc}$ projection, as displayed in Figs. 1(b) and 1(c). As demonstrated in Fig. 1(d), to insert F into the La_2CoO_4 lattice and obtain the intrinsic structure evolution, we placed a special La_2CoO_4 lamella with PVDF powders in the same quartz tube and heated it at 250 °C for 5 hours to obtain the oxyfluorides. The La_2CoO_4 lamella, which was milled into dimensions of 5×1 μm using focused ion beam (FIB) techniques, was subsequently mounted on a FIB support, with the final lamella thickness maintained below 50 nm. This setup can be directly transferred into the electron microscope, avoiding the negative effect caused by Ga ion irradiation in conventional atomic structure investigation.[31]

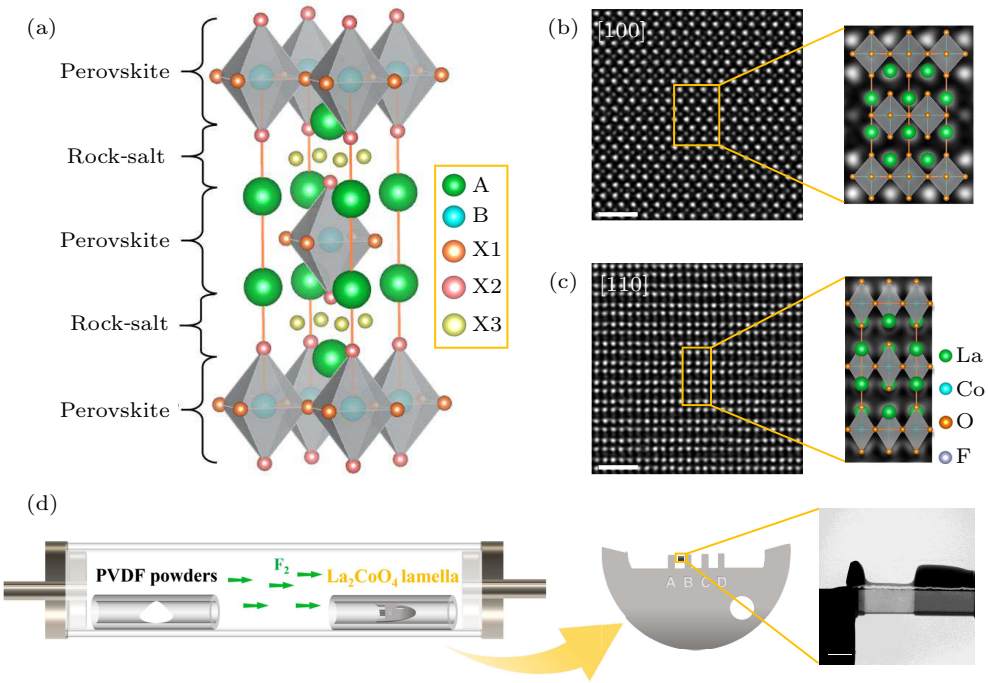


Fig. 1. Structural characteristics and fluorination process of La_2CoO_4. (a) The schematic diagram of the $n = 1$ RP-type structure includes perovskite layers and rock-salt layers, as well as three anion sites: equatorial (X1), apical (X2), and interstitial (X3). (b) High-angle annular dark (HAADF) image of La_2CoO_4 along the [100] and the enlarged image with overlayed structure model from the yellow-boxed area. Scale bar: 1 nm. (c) HAADF image of La_2CoO_4 along the [110] and the enlarged image with overlayed structure model from the yellow-boxed area. Scale bar: 1 nm. (d) Schematic diagram of the experimetal setup for low-temperature topotactic fluorination of La_2CoO_4, schematic diagram of the La_2CoO_4 lamella on a FIB support and low-magnification annular bright field (ABF) image of La_2CoO_4 lamella.

3.2. Atomic-scale lattice evolution under three fluorination states

We firstly acquired a series of high-angle annular dark-field (HAADF) images to investigate the structural evolution of La_2CoO_4 after low-temperature fluorination from regions with three fluorination stages. The La and Co columns can be visualized directly based on the Z contrast feature of HAADF images. The structural frameworks of both the pristine La_2CoO_4 and the oxyfluorides have been obtained, as shown in Figs. 2(a)–2(d). The impact of F insertion on the R-P lattice is visualized by mapping the intralayer La–La distance (d_{La-La}) projected along the $\langle 110 \rangle_{pc}$ direction. In the initial structure, the measured d_{La-La} are uniformly 2.8 Å (green). After fluorination, a large periodicity appears at stage I. The half d_{La-La} exhibit a checkerboard pattern of 2.3 Å (navy) and 3.4 Å (yellow), while the remaining regions retain the original 2.8 Å, corresponding to the presence of 4-fold superstructure diffraction points in the fast Fourier transform (FFT) pattern as displayed in the upper right corner of Fig. 2(b). With increasing F ions, the d_{La-La} exhibits a fully developed checkerboard pattern of 2.4 Å (navy) and 3.4 Å (yellow), in line with the 2-fold superstructure diffraction points in the FFT patterns at stages II and III (Figs. 2(c) and 2(d)).

The statistics of the lattice parameters at three fluorination stages are also summarized in Fig. 2(e). At stage I, the a-axis and c-axis elongations are 0.13 Å (from 5.46 Å to 5.59 Å) and 0.29 Å (from 12.25 Å to 12.54 Å), respectively, while the b-axis length remains almost unchanged. At stages II and III, the lengths of the a-axis and c-axis have slight elongations of 0.24 Å and 0.47 Å, respectively. During stage II, the length of the b-axis remains nearly constant, but it undergoes an elongation from 5.43 Å to 5.67 Å at stage III, becoming equal to the length of the a-axis. This structural evolution indicates that the crystal lattice undergoes distinct distortion modes as the fluorine content increases. The interplanar spacing maps of the lanthanum layer are used to measure the variations in the layer spacing of the perovskite and rock-salt layers as shown in Fig. S1, alternating navy and yellow/green stripes correspond to the rock-salt layers and perovskite layers, respectively. We can find that the elongation of c-axis in stages II and III is driven by the expansion of the perovskite layer (from 3.45 Å to 3.65 Å), while the rock-salt layers slightly contract. Previous studies reported that the insertion of fluoride ions into interstitial sites leads a strong elongation of the c axis in $La_2CoO_4F_{1.2}$ (from 12.6 Å to 15.3 Å)[28] and $LaSrMnO_4F$ (from 12.6 Å to 14 Å),[32] which is different from the situation in our La_2CoO_4 film. Thus, we speculate that the slight elongation in the c-axis (from 12.52 Å to 12.72 Å) is mainly caused by the tilting of the octahedron or substitution of the apical oxygen by the fluoride ion.[16,20] Meanwhile, the volume of oxyfluorides has linearly expanded from stage I to stage III with the F insertion, which indicates a nearly linear increase of F concentration in three stages.

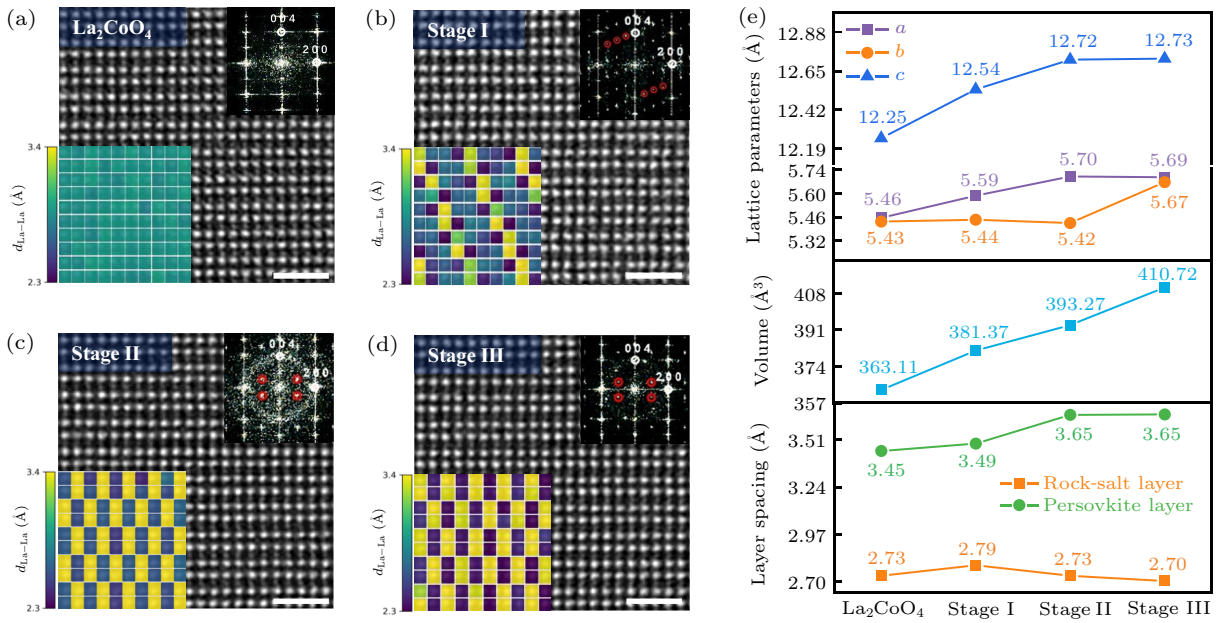


Fig. 2. Quantification analysis of lattice distortion in La_2CoO_4 and its oxyfluorides. (a)–(d) HAADF images of La_2CoO_4 in pristine state, stage I, stage II, and stage III along the $\langle 110 \rangle_{pc}$ zone axis. Scale bar: 1 nm. The insets in the lower left and upper right corners are the intralayer La–La distance maps of the lanthanum layers (d_{La-La}) and the fast Fourier transforms (FFT), respectively, reflecting the periodic distortions of the R-P lattice. Superstructure diffraction spots are highlighted with red circles. (e) Statistics of lattice constant, layer spacing and unit cell volume during the fluorination process.

3.3. Anion occupancy in oxyfluorides determined by EELS mapping

To obtain the oxygen/fluorine occupancy pattern of oxyfluorides, we performed atomically resolved STEM-EELS element maps. The direct electron detector (K3) with an exceptionally high signal-to-noise ratio is used for collecting EELS data to identify each element,[33,34] which provides an indispensable condition for visualizing the site occupancy of O/F. There exists an obvious F *K* edge absorption peak at 685 eV in stages II and III, proving that the appearance of the new structure is indeed caused by fluorination, as shown in Fig. S2. It should be noted that stage I was not stable due to the relatively high dose during the EELS acquisition. The peak positions of Co $L_{2,3}$ edges are stable after fluorination, indicating the unchanged valence state of Co^{2+}. The elemental maps for La $M_{4,5}$, Co $L_{2,3}$ and O *K* edges validate the uniform distribution of elements in the pristine La_2CoO_4 (Figs. 3(a), S3(a)–S3(e)), where equatorial and apical O in the perovskite layer are manifested clearly. As inferred above, the apical O completely disappears and is replaced by F in stage II (Figs. 3(b) and S3(f)–S3(j)). Meanwhile, part of the interstitial sites is occupied by O (indicated by yellow arrows). In stage III, besides the apical F, there is both O (indicated by yellow arrows) and F in the interstitial sites (Figs. 3(c) and S3(k)–S3(o)). Interestingly, the interstitial O in stages II and III alternately occupies interstitial anion sites within the rock-salt layer.

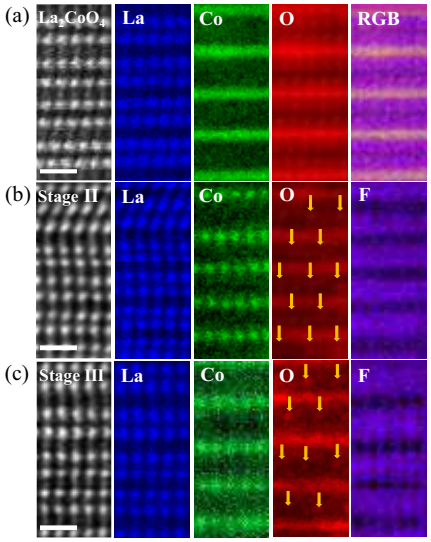


Fig. 3. The atomically resolved EELS elemental maps of La_2CoO_4 in pristine state, stage II, and stage III. HAADF image of La_2CoO_4 in pristine state (a), stage II (b) and stage III (c) along the $\langle 110 \rangle_{pc}$ zone axis, atomically resolved La, Co, O, F maps. The interstitial O are indicated by yellow arrows. Scale bar: 0.5 nm.

3.4. Regulation of $[Co(OF)_6]$ octahedral tilt by apical fluorine

To characterize the octahedral tilt evolution during fluorination, a series of annular bright field (ABF) images are acquired to demonstrate the anion occupancy due to its sensitivity to light anions such as O and F. Along the [110] zone axis, the $[CoO_6]$ tilt can be visualized directly as the vertical displacement of the equatorial oxygens. In the pristine La_2CoO_4, the $[CoO_6]$ tilt is nearly invisible with the empty interstitial sites, as shown in Figs. 4(a) and 4(e) in good agreement with the previous works.[35] In Fig. 4(b), stage I with anions exhibits an ordered 1/4 occupation in the interstitial layers (indicated by yellow dashed circles), and the half octahedra ex-

hibit significant tilting. The tilting of the octahedra between neighboring layers is antiphase, as shown in octahedral distortion model. The previous studies have reported that this distortion leads to form interstitial cavities with different sizes in the interstitial anion layer.[20,36–38] As shown in Fig. 4(c), in stage II, all octahedra exhibit significant tilting. Similar to stage I, through the antiphase tilting of octahedra between neighboring layers, interstitial cavities of different sizes are formed. There is an ordered full occupation of the interstitial anion layers and significant tilting of the octahedra in stage III (Fig. 4(d)). However, the interstitial sites display alternately strong (indicated by yellow dashed circles) and weak (indicated by red dashed circles) contrasts, which suggests ordered F and O occupancy in the rock-salt layers. A series of simulated ABF images are also acquired to validate the structural models, as shown in the lower-right corner of Figs. 4(b) and 4(d), which are in good agreement with the experimental images.

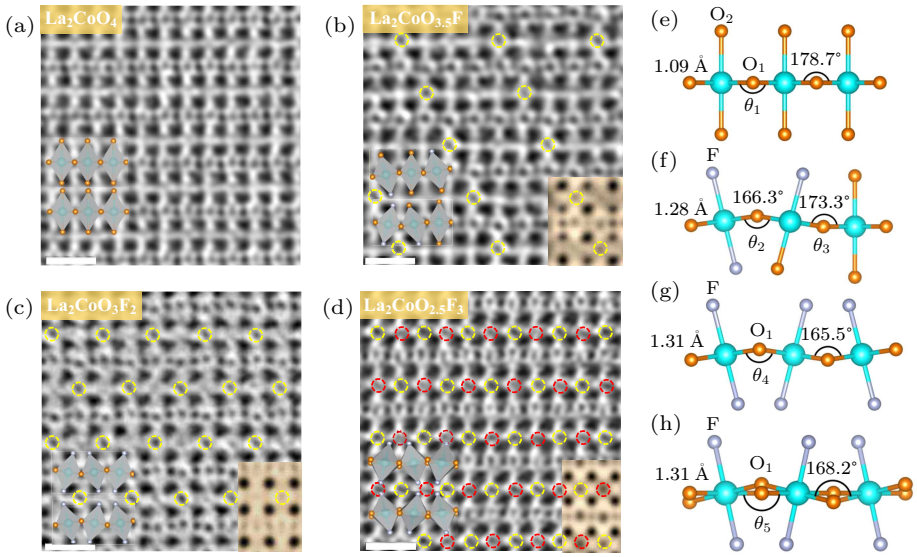


Fig. 4. Octahedral tilt of La_2CoO_4 and three oxyfluorides. (a)–(d) Annular bright field (ABF) images of the pristine La_2CoO_4, stage I ($La_2CoO_{3.5}F$), stage II ($La_2CoO_3F_2$), and stage III ($La_2CoO_{2.5}F_3$) along the [110] zone axis, respectively. Scale bar: 0.5 nm. The model in the lower left corner illustrates the octahedral distortion between neighboring layers. In stages I–III, the anions filling the interstitial sites are marked by yellow/red dashed circles, and simulated ABF images are shown in the lower right corner. (e)–(h) Corresponding Co–O_1–Co bond angles and Co–O_1 bond lengths of the octahedra in La_2CoO_4 and three oxyfluorides shown in (a)–(d).

To quantify the impact of fluorine substitution for apical oxygen on the tilt of the octahedra, we measured the Co–O_1–Co bond angles to gauge the degree of distortion of the octahedra. Figures S4(a)–S4(h) visually demonstrates the detailed process of measuring and statistically analyzing the Co–O_1–Co bond angles from ABF images. Note that bond angle θ_1 measured is 178.7° for pristine La_2CoO_4 (Fig. 4(e)), corresponding to the theoretical 180°. This discrepancy should be caused by the slight misalignment of the electron beam with respect to the crystal zone axis.[39] In stage I, two types of the bond angles can be identified: θ_2 being 166.3° near the interstitial anion sites and θ_3 being 173.3° at other sites (Figs. 4(b) and 4(f)). This variation is caused by the partially ordered substitution of the apical O by F, leading to a 6.7° tilting of the [$Co(OF)_6$] octahedra. Adjacent [$Co(OF)_6$] with antiphase tilting form the bond angle θ_2, while the [$Co(OF)_6$] adjacent to undistorted [CoO_6] form the bond angle θ_3. In stage II, the bond angles θ_4 are all 165.5° (Fig. 4(g)), indicating that F ions have completed the substitution of apical O, and the neighboring [CoO_4F_2] octahedra are tilted antiphase at an angle of approximately 7.2°. In stage III (Fig. 4(h)), the bond angles θ_5 are 168.2° with [CoO_4F_2] octahedra rotating by an angle of 5.9°, where interstitial fluorine induces the [CoO_4F_2] octahedra to tilt along the opposite direction, thus suppressing the magnitude of the overall octahedral tilt in the (110) plane, which will be shown later in this section. The variation in Co–O_1 bond length reflects the tetragonal elongation of the [$Co(OF)_6$] octahedra by the apical F.[40] As shown in Figs. 4(e) and 4(h), the initial projected Co–O_1 bond length is 1.09 Å, which gradually increases to 1.30 Å after fluorination.

The degree of octahedral distortion typically governs both multiferroic behavior[41] and magnetic ordering[42] in perovskite oxides. According to Glazer's notation, the octahedral distortion in stage II corresponds to the $a^-a^-c^0/a^-a^-c^0$ tilt system,[37] previously observed in R-P oxides like $La_{3.2}Ba_{0.8}Mn_3O_{10}$[36] and $Tb_2CaFe_2O_7$,[38] and has been extensively discussed in the $La_2NiO_3F_2$.[20] This creates alternating wide/narrow channels in rock-salt layers (Fig. S7(b)), with O^{2-} occupying wide channels, yielding an O/F ratio of 3:2 ($La_2CoO_3F_2$). In stage III, analogous to $La_2NiO_{2.5}F_3$, equivalent *a*- and *b*-axis elongation with full interstitial layer ordering indicates a distinct $a^-b^0c^0/b^0a^-c^0$ tilt system,[7,16] characterized by 90°-rotated octahedral tilts between $z = 0$ and $z = 1/2$ (Figs. S8(b) and S8(c)). This configuration generates

three large and one small interstitial site: two F^- occupy diagonal large sites, one O^{2-} fills the remaining large site, leaving the small site vacant (3/4 total occupancy). The resultant O/F ratio of 5:6 ($La_2CoO_{2.5}F_3$) aligns with the contrast variations in Fig. 3(d).

Additionally, the structural parameters of stage I, including the d_{La-La} lattice constant, Co–O_1–O bond angles and Co–O_1 bond lengths, are all intermediate between the initial La_2CoO_4 and $La_2CoO_3F_2$. The large-region ABF image in Fig. S5 shows that the crystal structure of stage I within the grains is not monophasic but intermixed with $La_2CoO_3F_2$. Thus, we deduce that stage I is an ordered transition structure, where F^- ions replace half of the apical O^{2-}, and this unique ordered substitution results in tilting of half of the octahedra. This, in turn, leads to a partial $a^-a^-c^0/a^-a^-c^0$ distortion, which creates a wide channel in the rock-salt layer every four interstitial sites to accommodate O^{2-}. Based on this filling pattern, the O/F ratio is determined to be 7:2, identifying this fluorinated oxide as $La_2CoO_{3.5}F$. Based on the $[Co(OF)_6]$ octahedral tilting shown in the ABF images and the O/F site occupancy shown in the elemental mapping, the structural evolution during topochemical fluorination of La_2CoO_4 has been summarized in Fig. S6.

3.5. Fine electronic structure evolution upon fluorination

To further elucidate the electronic evolution upon fluorination, we analyzed the fine structure of EELS spectra of La_2CoO_4, $LaCoO_3F_2$, and $La_2CoO_{2.5}F_3$ at atomic scale. Figure 5(a) displays the O *K* edge of pristine La_2CoO_4, which mainly exhibits three peaks labeled as A, B, and C. The pre-peak labeled A can be attributed to the hybridization of unoccupied Co 3d and O 2p orbitals, while peaks B and C originate from the hybridization of O 2p with La 5d and Co 4sp orbitals, respectively.[43] Compared to the initial structure, pre-peak A disappears in both oxyfluorides. Previous studies have attributed the suppressed pre-peak of the O *K* edge in perovskites to the formation of oxygen vacancies.[44,45] To clarify the origin of the disappearance of pre-peak A, we turned to measuring the Co $L_{2,3}$ edges, as shown in Fig. 5(b). No significant changes in the peak positions and L_3/L_2 ratio of Co $L_{2,3}$ edges suggest the unchanged oxidation state of Co^{2+}, excluding the possibility of oxygen vacancies. In fact, the substitution of apical O^{2-} by F^- annihilates the ligand holes in the Co $3d^8\underline{L}$ configuration through the introduction of dopant electrons,[46,47] resulting in the disappearance of pre-peak A.

Examining the B peak in the O *K* edge spectra, the 530 eV shoulder observed in pristine La_2CoO_4 (attributed to apical oxygen ligands via hybridization between O $2p_{x,y}$ and La 5d orbitals[46]) vanishes upon fluorination (Fig. 5(b)). This suppression directly correlates with the elimination of apical oxygen in the fluorinated structure. Conversely, a distinct 531 eV shoulder emerges in $La_2CoO_{2.5}F_3$. To investigate its origin, atomic-resolved spectra are obtained separately for the perovskite and rock-salt layers. As shown in Fig. 5(c), the 531 eV feature in $La_2CoO_{2.5}F_3$ exhibits pronounced enhancement within rock-salt layers, coinciding with interstitial oxygen, which indicates stronger hybridization between La 5d and interstitial oxygen 2p orbitals.

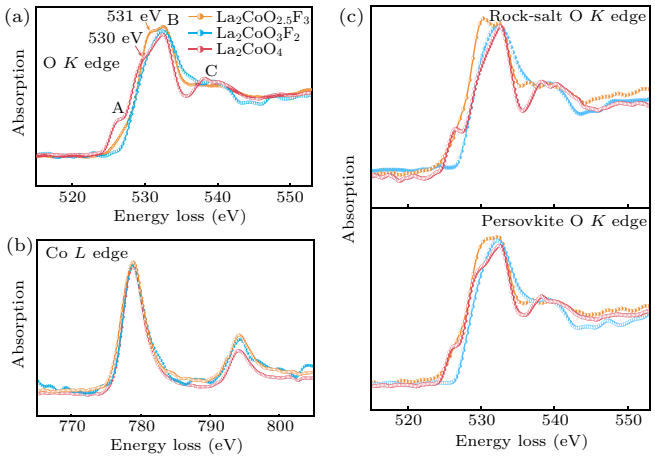


Fig. 5. The evolution in the fine structure of O *K* edge and Co *L* edge. (a) The oxygen *K* edge and (b) cobalt $L_{2,3}$ edge in La_2CoO_4, $La_2CoO_3F_2$ and $La_2CoO_{2.5}F_3$, respectively. The oxygen *K* edge spectra is categorized into pre-peak A and peaks B, C. (c) The O *K* edge EELS spectra were collected separately for the perovskite layers and the rock-salt layers.

4. Discussion

According to the crystal field splitting theory, the octahedral environment around the Co atoms allows the Co 3d states to split into lower t_{2g} states (i.e., d_{xy}, d_{yz}, d_{xz}) and higher e_g (i.e., $d_{x^2-y^2}$, d_{z^2}) states.[40,48] The in-plane elongation of the $[CoO_4F_2]$ octahedra lifts the degeneracy of t_{2g} into lower d_{xy} and higher d_{yz} and d_{xz} levels, whereas the e_g states split up into lower-energy $d_{x^2-y^2}$ and higher-energy d_{z^2}, as shown in Fig. S9. Thus, the fluorination would result in the lower-energy $d_{x^2-y^2}$ orbital and cause the magnetic moments to preferentially align within the CoO_2 plane, thereby further enhancing *XY*-like magnetic anisotropy.[49] This hypothesis has been experimentally confirmed in the axially elongated CoO_4X_2 system with the fact that the experimental magnetic moments (4.45 μ_B) are significantly higher than the spin-only magnetic moments (3 μ_B).[12] On the other hand, compared to the parent compound La_2NiO_4, the Néel temperature of the oxyfluoride $La_2NiO_3F_2$ is significantly reduced to 49 K.[20] This phenomenon suggests that substitution of apical O^{2-} with F^- critically weakens antiferromagnetic order in La_2CoO_4.

5. Conclusion

In conclusion, our comprehensive study utilizing aberration-corrected STEM and EELS has successfully elucidated the atomic-scale structural evolution of La_2CoO_4 dur-

ing topochemical fluorination, revealing three distinct ordered stages. A newly identified intermediate phase $La_2CoO_{3.5}F$ provided insights into the substitution dynamics. We directly observed F^- ions preferentially substituting apical oxygen sites, with displaced O^{2-} and excess F^- in interstitial positions. Apical F^- ions were found to critically influence octahedral tilt and cause significant changes in the fine-structure O *K* edge. The strong octahedral tilt leads to the in-plane elongation of the $[CoO_4F_2]$ octahedra. These findings not only provide atomic-level insights into the O/F exchange process but also highlight the pivotal role of fluorine in modulating octahedral tilt and electronic properties.

Acknowledgements

Project supported by the National Natural Science Foundation of China (Grant Nos. 52322212, 52025025, 52250402, and 12474001) and the National Key R&D Program of China (Grant Nos. 2022YFA1403203 and 2023YFA1406300).

References

[1] Wang T, Gong F, Ma X, Pan S, Wei X K, Kuo C, Yoshida S, Ku Y C, Wang S, Yang Z, Hazra S, Zhang K H L, Liu X, Tang Y, Zhu Y L, Chang C F, Das S, Ma X, Chen L, Xu B, Gopalan V, Bellaiche L, Martin L W and Chen Z 2025 *Sci. Adv.* **11** eads8830
[2] Sun X, Qin C, Zhao B, Jia S, Wang Z, Yang T, Liu X, Pan L, Zheng L, Luo D and Zhang Y 2024 *Energy Storage Materials* **70** 103559
[3] Hirai D 2024 *Inorganic Chemistry* **63** 4001
[4] Kasahara A, Nukumizu K, Hitoki G, Takata T, Kondo J N, Hara M, Kobayashi H and Domen K 2002 *J. Phys. Chem. A* **106** 6750
[5] Kobayashi G, Hinuma Y, Matsuoka S, Watanabe A, Iqbal M, Hirayama M, Yonemura M, Kamiyama T, Tanaka I and Kanno R 2016 *Science* **351** 1314
[6] Knee C S and Weller M T 2004 *Phys. Rev. B* **70** 144406
[7] Zhang R, Gibbs A S, Zhang W, Halasyamani P S and Hayward M A 2017 *Inorganic Chemistry* **56** 9988
[8] Zhang R, Senn M S and Hayward M A 2016 *Chemistry of Materials* **28** 8399
[9] Hartman S T, Cho S B and Mishra R 2018 *Inorganic Chemistry* **57** 10616
[10] Almamouri M, Edwards P P, Greaves C and Slaski M 1994 *Nature* **369** 382
[11] James A, Zahurak S M and Murphy D W 1989 *Nature* **338** 240
[12] Whangbo M H, Kremer R K and Koo H J 2022 *The Journal of Physical Chemistry C* **126** 16563
[13] Galasso F and Darby W 1963 *J. Phys. Chem.* **67** 1451
[14] Galasso F and Darby W 1962 *J. Phys. Chem.* **66** 1318
[15] Gonano B, Fjellvag O S, Steciuk G, Marshall K, Fjellvag H and Valldor M 2025 *Scripta Materialia* **255** 116379
[16] Jacobs J, Marques M A L, Wang H C, Dieterich E and Ebbinghaus S G 2021 *Inorganic Chemistry* **60** 13646
[17] Tsujimoto Y, Li J J, Yamaura K, Matsushita Y, Katsuya Y, Tanaka M, Shirako Y, Akaogi M and Takayama-Muromachi E 2011 *Chem. Commun.* **47** 3263
[18] Slater P R and Gover R K B 2002 *J. Mater. Chem.* **12** 291
[19] Sivakumar T and Wiley J B 2009 *Materials Research Bulletin* **44** 74
[20] Wissel K, Heldt J, Groszewicz P B, Dasgupta S, Breitzke H, Donzelli M, Waidha A I, Fortes A D, Rohrer J, Slater P R, Buntkowsky G and Clemens O 2018 *Inorganic Chemistry* **57** 6549
[21] Slater P R and Gover R K B 2001 *Journal of Materials Chemistry* **11** 2035
[22] Almamouri M, Edwards P P, Greaves C, Slater P R and Slaski M 1995 *Journal of Materials Chemistry* **5** 913
[23] Clemens O and Slater P R 2013 *Reviews in Inorganic Chemistry* **33** 105
[24] Wang Y, Salzberger U, Sigle W, Suyolcu Y E and van Aken P A 2016 *Ultramicroscopy* **168** 46
[25] Barthel J 2018 *Ultramicroscopy* **193** 1
[26] Tsujimoto Y, Yamaura K and Takayama-Muromachi E 2012 *Applied Sciences-Basel* **2** 206
[27] Li R K and Greaves C 2000 *Phys. Rev. B* **62** 3811
[28] Nowroozi M A, Ivlev S, Rohrer J and Clemens O 2018 *Journal of Materials Chemistry A* **6** 4658
[29] Meng Z, Yan H, Qin P, Yin Z, Jiang P, Zhou X, Wang X, Chen H, Liu L, Duan Z, Zhao G, Zhao W, Hu F, Zhang Q, Zhong Z and Liu Z 2024 *Nano Research* **17** 7250
[30] Lin T, Gao A, Tang Z, Lin W, Sun M, Zhang Q, Wang X, Guo E J and Gu L 2024 *Chin. Phys. Lett.* **41** 047701
[31] Li H, Daukiya L, Haldar S, Lindblad A, Sanyal B, Eriksson O, Aubel D, Hajjar-Garreau S, Simon L and Leifer K 2016 *Scientific Reports* **6** 19719
[32] Aikens L D, Li R K and Greaves C 2000 *Chem. Commun.* 2129
[33] Susarla S, Garcia-Fernandez P, Ophus C, Das S, Aguado-Puente P, McCarter M, Ercius P, Martin L W, Ramesh R and Junquera J 2021 *Nat. Commun.* **12** 6273
[34] Zachman M J, Serov A, Lyu X, McKinney S, Yu H, Oxley M P, Spillane L, Holby E F and Cullen D A 2023 *Electrochimica Acta* **469** 143205
[35] Hong Y, Byeon P, Bak J, Heo Y, Kim H S, Bae H B and Chung S Y 2021 *Nat. Commun.* **12** 5527
[36] Hadermann J, Abakumov A, Tsirlin A A, Rozova M G, Sarakinou E and Antipov E V 2012 *Inorganic Chemistry* **51** 11487
[37] Aleksandrov K S and Bartolomé J 2001 *Phase Transitions* **74** 255
[38] Pitcher M J, Mandal P, Dyer M S, Alaria J, Borisov P, Niu H, Claridge J B and Rosseinsky M J 2015 *Science* **347** 420
[39] Zhou D, Mueller-Caspary K, Sigle W, Krause F F, Rosenauer A and van Aken P 2016 *Ultramicroscopy* **160** 110
[40] Khomskii D I and Streltsov S V 2021 *Chemical Reviews* **121** 2992
[41] Liang G, Cao H, Cheng L, Zha J, Bao M, Ye F, Zhou H, Zhao A and Zhai X 2024 *Chin. Phys. B* **33** 097101
[42] Fan Y Y, Wang J, Hu F X, Li B H, Geng A C, Yin Z, Zhang C, Zhou H B, Wang M Q, Yu Z B and Shen B G 2023 *Chin. Phys. B* **32** 087504
[43] Frati F, Hunault M O J Y and de Groot F M F 2020 *Chem. Rev.* **120** 4056
[44] Li D, Wang H, Li K, Zhu B, Jiang K, Backes D, Veiga L S I, Shi J, Roy P, Xiao M, Chen A, Jia Q, Lee T L, Dhesi S S, Scanlon D O, MacManus-Driscoll J L, van Aken P A, Zhang K H L and Li W 2023 *Nat. Commun.* **14** 3638
[45] Mehta V V, Biskup N, Jenkins C, Arenholz E, Varela M and Suzuki Y 2015 *Phys. Rev. B* **91** 144418
[46] Dong Z, Huo M, Li J, Li J, Li P, Sun H, Gu L, Lu Y, Wang M, Wang Y and Chen Z 2024 *Nature* **630** 847
[47] Li D, Wang H, Li K, Zhu B, Jiang K, Backes D, Veiga L S I, Shi J, Roy P, Xiao M, Chen A, Jia Q, Lee T L, Dhesi S S, Scanlon D O, MacManus-Driscoll J L, van Aken P A, Zhang K H L and Li W 2023 *Nat. Commun.* **14** 3638
[48] Kim W J, Smeaton M A, Jia C, Goodge B H, Cho B G, Lee K, Osada M, Jost D, Ievlev A V, Moritz B, Kourkoutis L F, Devereaux T P and Hwang H Y 2023 *Nature* **615** 237
[49] Babkevich P, Prabhakaran D, Frost C D and Boothroyd A T 2010 *Phys. Rev. B* **82** 184425